

Suppression of photon shot noise dephasing in a tunable coupling superconducting qubit

Gengyan Zhang, Yanbing Liu, James J. Raftery, Andrew A. Houck*

Department of Electrical Engineering, Princeton University, Princeton, New Jersey 08544, USA.

We demonstrate the suppression of photon shot noise dephasing in a superconducting qubit by eliminating its dispersive coupling to the readout cavity. This is achieved in a tunable coupling qubit, where the qubit frequency and coupling rate can be controlled independently. We observe that the coherence time approaches twice the relaxation time and becomes less sensitive to thermal photon noise when the dispersive coupling rate is tuned from several MHz to 22 kHz. This work provides a promising building block in circuit quantum electrodynamics that can hold high coherence and be integrated into larger systems.

INTRODUCTION

Superconducting quantum circuits are a strong candidate for quantum computing [1–3] and a convenient platform for quantum optics [4–6] and quantum simulation [7, 8]. Extensive efforts have been made in the last decade to isolate these quantum systems from various decay channels and noise sources in the environment, leading to an increase of several orders of magnitude in energy relaxation time T_1 and phase coherence time T_2 (ref. 9). State-of-the-art devices have achieved T_1 and T_2 in the millisecond regime [10, 11] and pushed gate fidelity close to the threshold for fault-tolerant quantum computing [12]. However, the progress in T_2 is slower than that in T_1 and T_2/T_1 ratios in these devices fall in the range between 0.5 and 1.5 (refs. 10, 13, and 14). Deviation from the theoretical limit of $T_2 = 2T_1$ indicates dephasing mechanisms that need to be understood and circumvented.

In circuit quantum electrodynamics (cQED) [15, 16], manipulation and readout of a superconducting qubit are mediated by its coupling to a transmission line cavity. When the coupling is dispersive, photons in the cavity can be utilized to measure the qubit if their phase is shifted by a distinguishable amount depending on the qubit state. On the other hand, changes in cavity photon number will shift the qubit frequency due to the same coupling mechanism. When the amount of the frequency shift is large enough, thermal or quantum fluctuations of cavity photons lead to dephasing of the qubit. This photon shot noise dephasing mechanism has been studied theoretically [17] and experimentally [14] and has become a dominant factor that limits the coherence time of superconducting qubits. The qualitative discussion above indicates that the dephasing can be suppressed by reducing (1) the photon number fluctuation, characterized by cavity decay rate κ , (2) the thermal photon population n_{th} , and (3) the frequency shift caused by each photon, characterized by the dispersive coupling rate χ . Most work in the past has adopted the first two strategies and used high Q ($> 10^6$) 3D cavities [10, 18] and careful filtering and thermal anchoring to reduce κ and n_{th}

(refs. 14 and 19). Here we focus on the third approach and demonstrate the suppression of photon shot noise dephasing when χ is tuned to near zero. This is realized in a tunable coupling qubit (TCQ) [20, 21], where the qubit frequency and coupling strength can be tuned independently [22]. Moreover, we show that measurement of the qubit state can still be performed conveniently when $\chi \ll \kappa$.

In this paper, we start with spectroscopic measurements on the TCQ to demonstrate the independent tunability of its frequency and dispersive coupling rate. We achieve χ as low as 22 kHz when the dispersive interaction of two different qubit modes is tuned to cancel each other. Next we show that readout of the qubit state near the zero- χ regime can be realized by utilizing a higher energy level. Finally, we perform time domain measurements of T_1 and T_2 with injected noise and demonstrate the robustness of T_2 against photon shot noise when χ is near zero.

RESULTS

The TCQ, shown in Fig. 1a, consists of two transmon qubits [23] strongly coupled to each other via a common third island. The geometry of the islands are designed to minimize the electric participation ratios in the material interfaces and reduce bulk and surface losses of the qubit [24]. The two transmons are formed by capacitively shunted SQUID loops and their frequencies can be tuned by two DC voltages applied to the local magnetic flux bias lines. The strong coupling between the transmon states causes their hybridization and results in a V-shaped energy diagram shown in Fig. 1b. The one-excitation manifold contains two collective qubit states whose frequencies ω_{\pm} and dipole coupling rates g_{\pm} can be tuned as a function of the two flux biases. Tunable coupling originates from the interference between the dipole moments of the two transmons and provides an extra degree of freedom compared to standard transmon qubits. The two-excitation states acquire different self and cross anharmonicities α_{\pm} and α_c due to the hy-

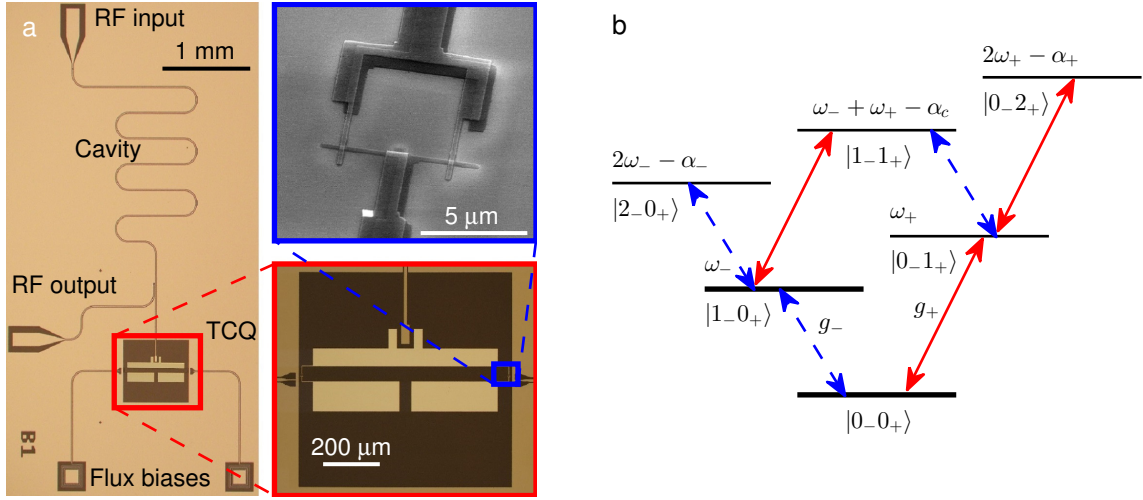


FIG. 1. TCQ device and its energy levels. (a) Optical micrographs show a TCQ coupled to the end of a readout cavity. RF input and output ports are coupled capacitively to the cavity and spiral inductors are used as low pass filters for the DC bias lines. Electron micrograph shows two Josephson junctions forming a SQUID loop of size $\approx 5 \times 5 \mu\text{m}^2$. (b) V-shaped energy diagram up to two qubit excitations. Red solid and blue dashed lines indicate transitions with dipole coupling rates g_+ and g_- respectively.

bridization, which allows us to drive a desired transition between two states (indicated by arrows in Fig. 1b) without causing other unwanted transitions. A coplanar waveguide (CPW) cavity with resonance frequency $\omega_r/2\pi = 7.14$ GHz and linewidth $\kappa/2\pi = 250$ kHz is capacitively coupled to the TCQ to drive and read out the qubit states.

We operate the TCQ in the dispersive regime, where the qubit-cavity detunings $|\Delta_{\pm}| = |\omega_{\pm} - \omega_r| \gg |g_{\pm}|$, and the Hamiltonian of the device can be approximated by

$$\begin{aligned} \frac{H}{\hbar} &= \omega_r a^\dagger a + \omega_- b_-^\dagger b_- + \omega_+ b_+^\dagger b_+ \\ &+ \chi_- a^\dagger ab_-^\dagger b_- + \chi_+ a^\dagger ab_+^\dagger b_+ \\ &- \frac{\alpha_-}{2} b_-^\dagger b_-^\dagger b_- b_- - \frac{\alpha_+}{2} b_+^\dagger b_+^\dagger b_+ b_+ - \alpha_c b_-^\dagger b_- b_+^\dagger b_+. \end{aligned} \quad (1)$$

Here a, b_{\pm} denote the annihilation operators for the cavity and qubit modes, and χ_{\pm} are the dispersive coupling rates between the qubits and the cavity. The measured values for the parameters are $\omega_-/2\pi = 7.25$ GHz, $0 \lesssim g_-/2\pi < 10$ MHz, $\omega_+/2\pi \approx 9.80$ GHz, $g_+/2\pi \approx 90$ MHz, $\alpha_-/2\pi = 129$ MHz, $\alpha_+/2\pi = 239$ MHz, and $\alpha_c/2\pi = 358$ MHz. In this work, we use the ground ($|0_-0_+\rangle$) and first excited ($|1_-0_+\rangle$) states as the computational basis, so the logical qubit has frequency ω_- and dispersive coupling rate χ_- . The tunability of χ_- can be seen from its explicit expression derived in ref. 20 using second order perturbation theory,

$$\begin{aligned} \chi_- &= \chi_1 + \chi_2 \\ &= \frac{2g_-^2 \alpha_-}{\Delta_- (\alpha_- - \Delta_-)} + \frac{g_+^2 \alpha_c}{\Delta_+ (\alpha_c - \Delta_+)}, \end{aligned} \quad (2)$$

where $\chi_{1,2}$ correspond to contributions from the two collective qubit states. The ability to vary g_{\pm} in addition to Δ_{\pm} allows us to tune χ_- in a flexible way. In particular, when we tune one qubit into the straddling regime [23, 25] and the other far above the cavity, i.e., $g_- \ll \Delta_- < \alpha_-$ and $\Delta_+ \gg \max(\alpha_c, g_+)$, χ_1 and χ_2 have opposite signs and χ_- reaches zero when they cancel each other. In the experiment, we fix Δ_- and use g_- as the main control knob to tune χ_- : When g_- is large enough, $\chi_1 > |\chi_2|$ and χ_- is positive; As we tune down g_- , χ_1 decreases and χ_- becomes negative when $\chi_1 < |\chi_2|$.

Figure 2 shows the measured data for tunable χ_- . Standard qubit spectroscopy measurement is repeated for different combinations of the two flux biases (Φ_1, Φ_2) to map out the constant ω_- contour in Fig. 2a. Here, Φ_1 is varied linearly and Φ_2 (not shown in the figure) is determined by the condition that $\omega_-/2\pi$ remains 7.25 GHz when the intracavity photon number \bar{n} is small. Along the contour, the phase shift of the cavity transmission changes sign, indicating that χ_- crosses zero. For larger \bar{n} , the qubit frequency is dressed by cavity photons and exhibits an ac Stark shift [26] of $\bar{n}\chi_-$. The dressed qubit frequency in Fig. 2b shows clearly that χ_- can be tuned to be both positive and negative, from a few MHz down to below the cavity linewidth $\kappa/2\pi = 250$ kHz, which cannot be resolved in the qubit spectroscopy.

As χ_- approaches zero, so does the readout contrast because there is no dispersive shift caused by the $|1_-0_+\rangle$ state, as is illustrated in Fig. 2 near $\Phi_1 = -0.95$. To achieve efficient readout for small χ_- , we adopt a scheme that utilizes a third state $|1_-1_+\rangle$. In this scheme, we apply a transfer pulse at frequency $\omega_+ - \alpha_c$ to the TCQ, inducing a $|1_-0_+\rangle \rightarrow |1_-1_+\rangle$ transition, imme-

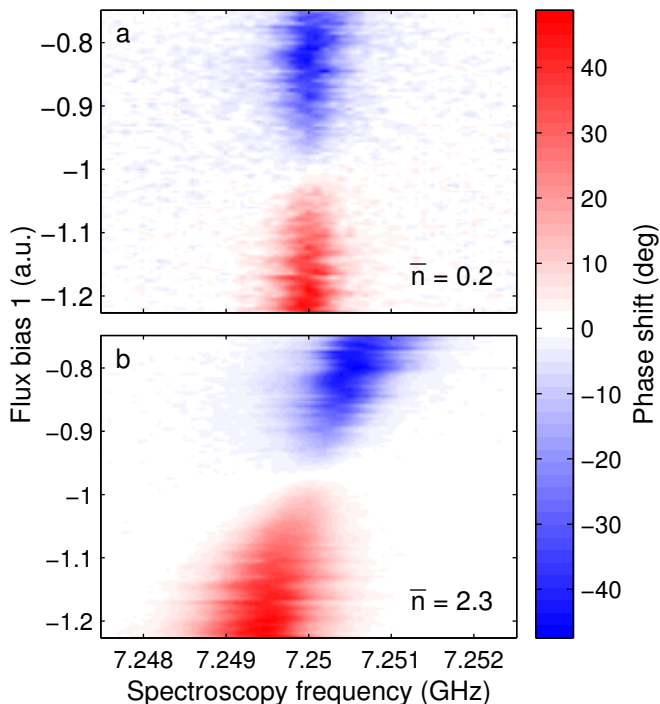


FIG. 2. Tunable dispersive coupling. Phase shift of the cavity transmission is monitored when a second spectroscopy tone sweeps around the qubit frequency. (a) Qubit frequency is fixed at 7.25 GHz when intracavity photon number $\bar{n} = 0.2$. The phase shift switches sign when χ_- crosses zero. (b) When $\bar{n} = 2.3$, upward (downward) ac Stark shift of the qubit frequency illustrates positive (negative) χ_- . The spectroscopy signal vanishes near $V_1 = -0.95$ V, where χ_- approaches zero.

diately before the readout pulse at frequency ω_r . The $|1_{-1+}\rangle$ state provides a measured dispersive shift of -1.2 MHz around the zero χ_- point and can be used to indirectly read out the logical qubit state. To test this readout method, we prepare the logical qubit to a state $|\psi\rangle$ characterized by Rabi angle θ_1 , i.e., $|\psi\rangle = \cos(\theta_1/2)|0_{-0+}\rangle + \sin(\theta_1/2)|1_{-0+}\rangle$, by sending a Gaussian pulse at frequency ω_- . A transfer pulse with Rabi angle θ_2 is then applied as described above, followed by the readout pulse. The widths of the Gaussian pulses are fixed at $\sigma = 16$ ns and $\theta_{1,2}$ are controlled by the pulse amplitudes. Figure 3a shows the measured homodyne signal at $\chi_- \approx 0$ as a function of θ_1 and θ_2 . Rabi oscillations for both $|0_{-0+}\rangle \leftrightarrow |1_{-0+}\rangle$ and $|1_{-0+}\rangle \leftrightarrow |1_{-1+}\rangle$ transitions are observed, demonstrating coherent transfers between the quantum states. In the absence of the transfer pulse, no visible contrast is observed because of small χ_- (blue dots in Fig. 3b). As the amplitude of the transfer pulse is adjusted to $\theta_2 = \pi$, $|\psi\rangle$ is transferred to $|\psi'\rangle = \cos(\theta_1/2)|0_{-0+}\rangle + \sin(\theta_1/2)|1_{-1+}\rangle$, which gives the maximum readout contrast (red crosses in Fig. 3b) and recovers the Rabi angle θ_1 . This method allows for the single qubit control and readout scheme to be performed entirely with microwave pulses, and does not in-

volve dynamical tuning of χ_- via fast flux biasing, which increases experimental complexity and might cause unwanted qubit errors. It also allows low pass filtering to reduce the Purcell decay of the qubit through the flux bias lines [27, 28].

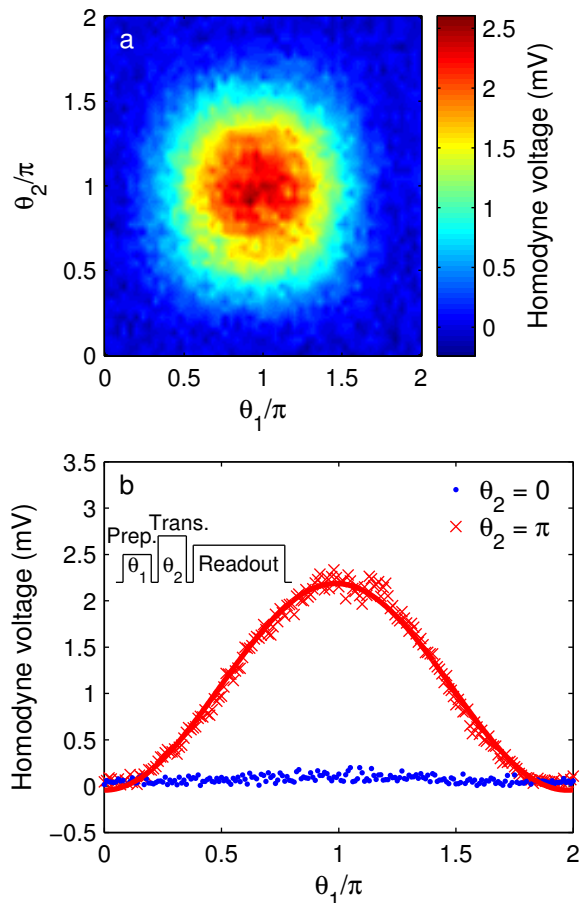


FIG. 3. Qubit readout when $\chi_- \approx 0$. Two consecutive Gaussian pulses with $\sigma = 16$ ns and frequencies ω_- , $\omega_+ - \alpha_c$ are sent to drive qubit transitions, followed by a readout pulse at the cavity frequency ω_r . (a) Homodyne readout signal shows Rabi oscillations for both $|0_{-0+}\rangle \leftrightarrow |1_{-0+}\rangle$ and $|1_{-0+}\rangle \leftrightarrow |1_{-1+}\rangle$ transitions, with Rabi angles $\theta_{1,2}$ determined by the amplitudes of the two drive pulses. (b) Horizontal cuts at $\theta_2 = 0$ and π in (a). Maximum readout contrast (red crosses) is obtained after transferring $|1_{-0+}\rangle$ to $|1_{-1+}\rangle$ by a transfer pulse with $\theta_2 = \pi$, in contrast to very low readout signal (blue dots) with no transfer pulse. The pulse sequence is shown in the inset.

Combining the tunability of χ_- and the readout method, we perform time domain measurements for the qubit relaxation and coherence time. In addition to the standard measurement setup, we use a noise source to study the influence of thermal photon fluctuations on qubit dephasing. White noise within the bandwidth 7.1375 GHz \pm 5 MHz is injected to the device, covering the cavity but not the qubit, and its power density determines the intracavity noise photon number n_{th} . In

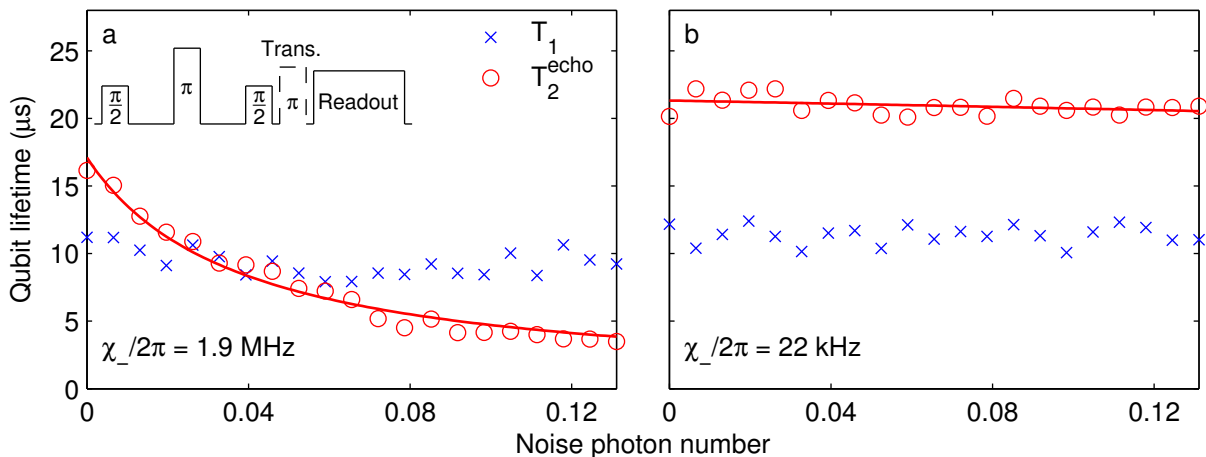


FIG. 4. Qubit relaxation time T_1 (blue crosses), dephasing time T_2 with Hahn echo (red dots) and fit to equation (3) (red curves) as a function of injected photon noise. (a) When $\chi_-/2\pi = 1.9$ MHz, T_2 drops from $16 \mu\text{s}$ to $3.5 \mu\text{s}$ with increasing photon noise. Inset: pulse sequence for T_2 measurement with (without) a transfer pulse for small (large) χ_- . (b) When $\chi_-/2\pi = 22$ kHz, no drop in T_2 is observed up to noise photon number $n_{\text{th}} = 0.13$.

Fig. 4a, the measured T_1 and T_2 for $\chi_-/2\pi = 1.9$ MHz are plotted as a function of the injected noise power. A Hahn echo pulse is used in measuring T_2 to eliminate slow dephasing processes caused by flux noise, etc. While T_1 exhibits little dependence on the injected noise and remains $8 \sim 11 \mu\text{s}$, T_2 drops from $16 \mu\text{s}$ to $3.5 \mu\text{s}$ as the noise power increases, reflecting a photon shot noise limited T_2 when χ_- is comparable to χ used in normal transmon devices. Figure 4b shows the result for the same measurements when $\chi_- \approx 0$ and we obtain $T_1 = 10 \sim 12 \mu\text{s}$ and $T_2 = 20 \sim 22 \mu\text{s}$, and no reduction is observed in either T_1 or T_2 up to $n_{\text{th}} = 0.13$. To quantitatively analyze the result, we use the analytic expression for photon shot noise dephasing rate Γ_ϕ derived in refs. 14 and 29,

$$\Gamma_\phi = \frac{\kappa}{2} \text{Re} \left[\sqrt{\left(1 + \frac{i\chi_-}{\kappa}\right)^2 + \frac{4i\chi_- n_{\text{th}}}{\kappa}} - 1 \right], \quad (3)$$

and fit the measured T_2 data to equation (3), shown in the red curves in Fig. 4. In Fig. 4a, a single linear fitting parameter converts the output power of the noise source to the n_{th} values in the x axis; In Fig. 4b we extract $\chi_-/2\pi = 22$ kHz from the best fit to equation (3).

DISCUSSION

To estimate Γ_ϕ , we assume a typical $n_{\text{th}} = 0.02$ (refs. 14 and 26). The small χ_- leads to $\Gamma_\phi = 0.25$ kHz, corresponding to a photon shot noise limited T_2 of $4000 \mu\text{s}$. In comparison, to achieve the same level of Γ_ϕ with the same n_{th} in a high Q cavity device would require $\kappa/2\pi = 2$ kHz ($Q \sim 3 \times 10^6$). The T_1 of the device is Purcell limited [27] because of the small detuning between the qubit and cavity, evidenced by a measured

$T_1 = 21 \mu\text{s}$ when tuning the qubit to 2.2 GHz below the cavity, and can be improved by increasing cavity Q or engineering the cavity spectrum using filters [28, 30].

Compared to other methods to suppress photon shot noise dephasing, our approach does not rely on very high Q cavities and T_2 is limited by χ_- , which in principle can be tuned to zero. Gate operation and readout can be performed conveniently without dynamical control of the qubit. The planar geometry also makes it easy to integrate the device into larger cQED systems. Potential applications in multi-qubit devices include using the TCQ as coupling bus between two transmon qubits to reduce/enhance their cross coupling strength. The ability to access and measure the quantum state while maintaining the high coherence makes the TCQ a promising building block for the processing and storage of quantum information.

METHODS

The device is fabricated on a $500\text{-}\mu\text{m}$ -thick sapphire substrate. The CPW cavity is defined using photolithography and reactive ion etching of a 200 nm film of niobium sputtered on the sapphire. The TCQ is patterned using electron beam lithography and the Josephson junctions are made using bridge-free, double-angle evaporation [31]. The chip is mounted and wire bonded to a printed circuit board and cooled down to ~ 10 mK in a dilution refrigerator. Input signals generated at room temperature are attenuated and filtered at different stages of the refrigerator. Output signals are amplified at 4 K and room temperature and acquired by a high-speed digitizer.

ACKNOWLEDGEMENTS

This work is supported by IARPA under contract W911NF-10-1-0324.

COMPETING INTERESTS

The authors declare no conflict of interest.

* aahouck@princeton.edu

- [1] M. D. Reed, L. DiCarlo, S. E. Nigg, L. Sun, L. Frunzio, S. M. Girvin, and R. J. Schoelkopf, *Nature* **482**, 382 (2012).
- [2] E. Lucero, R. Barends, Y. Chen, J. Kelly, M. Mariantoni, A. Megrant, P. O'Malley, D. Sank, A. Vainsencher, J. Wenner, T. White, Y. Yin, A. N. Cleland, and J. M. Martinis, *Nature Phys.* **8**, 719 (2012).
- [3] A. D. Córcoles, E. Magesan, S. J. Srinivasan, A. W. Cross, M. Steffen, J. M. Gambetta, and J. M. Chow, *Nat. Commun.* **6**, 6979 (2015).
- [4] A. A. Houck, D. I. Schuster, J. M. Gambetta, J. A. Schreier, B. R. Johnson, J. M. Chow, L. Frunzio, J. Majer, M. H. Devoret, S. M. Girvin, and R. J. Schoelkopf, *Nature* **449**, 328 (2007).
- [5] M. Hofheinz, H. Wang, M. Ansmann, R. C. Bialczak, E. Lucero, M. Neeley, A. D. O'Connell, D. Sank, J. Wenner, J. M. Martinis, and A. N. Cleland, *Nature* **459**, 546 (2009).
- [6] G. Kirchmair, B. Vlastakis, Z. Leghtas, S. E. Nigg, H. Paik, E. Ginossar, M. Mirrahimi, L. Frunzio, S. M. Girvin, and R. J. Schoelkopf, *Nature* **495**, 205 (2013).
- [7] A. A. Houck, H. E. Türeci, and J. Koch, *Nature Phys.* **8**, 292 (2012).
- [8] S. Schmidt and J. Koch, *Ann. Phys.* **525**, 395 (2013).
- [9] M. H. Devoret and R. J. Schoelkopf, *Science* **339**, 1169 (2013).
- [10] M. Reagor, W. Pfaff, C. Axline, R. W. Heeres, N. Ofek, K. Sliwa, E. Holland, C. Wang, J. Blumoff, K. Chou, M. J. Hatridge, L. Frunzio, M. H. Devoret, L. Jiang, and R. J. Schoelkopf, *Phys. Rev. B* **94**, 014506 (2016).
- [11] I. M. Pop, K. Geerlings, G. Catelani, R. J. Schoelkopf, L. I. Glazman, and M. H. Devoret, *Nature* **508**, 369 (2014).
- [12] R. Barends, J. Kelly, A. Megrant, A. Veitia, D. Sank, E. Jeffrey, T. C. White, J. Mutus, A. G. Fowler, B. Campbell, Y. Chen, Z. Chen, B. Chiaro, A. Dunsworth, C. Neill, P. O'Malley, P. Roushan, A. Vainsencher, J. Wenner, A. N. Korotkov, A. N. Cleland, and J. M. Martinis, *Nature* **508**, 500 (2014).
- [13] H. Paik, D. I. Schuster, L. S. Bishop, G. Kirchmair, G. Catelani, A. P. Sears, B. R. Johnson, M. J. Reagor, L. Frunzio, L. I. Glazman, S. M. Girvin, M. H. Devoret, and R. J. Schoelkopf, *Phys. Rev. Lett.* **107**, 240501 (2011).
- [14] C. Rigetti, J. M. Gambetta, S. Poletto, B. L. T. Plourde, J. M. Chow, A. D. Córcoles, J. A. Smolin, S. T. Merkel, J. R. Rozen, G. A. Keefe, M. B. Rothwell, M. B. Ketchen, and M. Steffen, *Phys. Rev. B* **86**, 100506 (2012).
- [15] A. Blais, R. S. Huang, A. Wallraff, S. M. Girvin, and R. J. Schoelkopf, *Phys. Rev. A* **69**, 062320 (2004).
- [16] A. Wallraff, D. I. Schuster, A. Blais, L. Frunzio, R. S. Huang, J. Majer, S. Kumar, S. M. Girvin, and R. J. Schoelkopf, *Nature* **431**, 162 (2004).
- [17] J. Gambetta, A. Blais, D. I. Schuster, A. Wallraff, L. Frunzio, J. Majer, M. H. Devoret, S. M. Girvin, and R. J. Schoelkopf, *Phys. Rev. A* **74**, 042318 (2006).
- [18] A. P. Sears, A. Petrenko, G. Catelani, L. Sun, H. Paik, G. Kirchmair, L. Frunzio, L. I. Glazman, S. M. Girvin, and R. J. Schoelkopf, *Phys. Rev. B* **86**, 180504 (2012).
- [19] X. Y. Jin, A. Kamal, A. P. Sears, T. Gudmundsen, D. Hover, J. Miloshi, R. Slattery, F. Yan, J. Yoder, T. P. Orlando, S. Gustavsson, and W. D. Oliver, *Phys. Rev. Lett.* **114**, 240501 (2015).
- [20] J. M. Gambetta, A. A. Houck, and A. Blais, *Phys. Rev. Lett.* **106**, 030502 (2011).
- [21] S. J. Srinivasan, A. J. Hoffman, J. M. Gambetta, and A. A. Houck, *Phys. Rev. Lett.* **106**, 083601 (2011).
- [22] A. J. Hoffman, S. J. Srinivasan, J. M. Gambetta, and A. A. Houck, *Phys. Rev. B* **84**, 184515 (2011).
- [23] J. Koch, T. M. Yu, J. Gambetta, A. A. Houck, D. I. Schuster, J. Majer, A. Blais, M. H. Devoret, S. M. Girvin, and R. J. Schoelkopf, *Phys. Rev. A* **76**, 042319 (2007).
- [24] O. Dial, D. T. McClure, S. Poletto, G. A. Keefe, M. B. Rothwell, J. M. Gambetta, D. W. Abraham, J. M. Chow, and M. Steffen, *Supercond. Sci. Technol.* **29**, 044001 (2016).
- [25] K. Inomata, T. Yamamoto, P.-M. Billangeon, Y. Nakamura, and J. S. Tsai, *Phys. Rev. B* **86**, 140508 (2012).
- [26] D. I. Schuster, A. Wallraff, A. Blais, L. Frunzio, R. S. Huang, J. Majer, S. M. Girvin, and R. J. Schoelkopf, *Phys. Rev. Lett.* **94**, 123602 (2005).
- [27] A. A. Houck, J. A. Schreier, B. R. Johnson, J. M. Chow, J. Koch, J. M. Gambetta, D. I. Schuster, L. Frunzio, M. H. Devoret, S. M. Girvin, and R. J. Schoelkopf, *Phys. Rev. Lett.* **101**, 080502 (2008).
- [28] M. D. Reed, B. R. Johnson, A. A. Houck, L. DiCarlo, J. M. Chow, D. I. Schuster, L. Frunzio, and R. J. Schoelkopf, *Appl. Phys. Lett.* **96**, 203110 (2010).
- [29] A. A. Clerk and D. W. Utami, *Phys. Rev. A* **75**, 042302 (2007).
- [30] N. T. Bronn, Y. Liu, J. B. Hertzberg, A. D. Córcoles, A. A. Houck, J. M. Gambetta, and J. M. Chow, *Appl. Phys. Lett.* **107**, 172601 (2015).
- [31] A. Potts, G. J. Parker, J. J. Baumberg, and P. A. J. de Groot, *IEE Proc., Sci. Meas. Technol.* **148**, 225 (2001).